APPLIED SCIENCES AND ENGINEERING

Mantis shrimp–inspired organic photodetector for simultaneous hyperspectral and polarimetric imaging

Ali Altaqui[1], Pratik Sen[2], Harry Schrickx[2], Jeromy Rech[3], Jin-Woo Lee[4], Michael Escuti[1], Wei You[3], Bumjoon J. Kim[4], Robert Kolbas[1], Brendan T. O'Connor[2]*, Michael Kudenov[1]*

Combining hyperspectral and polarimetric imaging provides a powerful sensing modality with broad applications from astronomy to biology. Existing methods rely on temporal data acquisition or snapshot imaging of spatially separated detectors. These approaches incur fundamental artifacts that degrade imaging performance. To overcome these limitations, we present a stomatopod-inspired sensor capable of snapshot hyperspectral and polarization sensing in a single pixel. The design consists of stacking polarization-sensitive organic photovoltaics (P-OPVs) and polymer retarders. Multiple spectral and polarization channels are obtained by exploiting the P-OPVs' anisotropic response and the retarders' dispersion. We show that the design can sense 15 spectral channels over a 350-nanometer bandwidth. A detector is also experimentally demonstrated, which simultaneously registers four spectral channels and three polarization channels. The sensor showcases the myriad degrees of freedom offered by organic semiconductors that are not available in inorganics and heralds a fundamentally unexplored route for simultaneous spectral and polarimetric imaging.

INTRODUCTION

Spectral polarization imaging (SPI) is a four-dimensional (4D) measurement technique that acquires the spatial, spectral, and polarimetric information of a scene (*1*). This state-of-the-art imaging method has the potential to revolutionize many fields, ranging from agriculture and medicine to defense and space exploration (*2*). In particular, SPI plays a crucial role in biomedical imaging, such as diagnosing human cancerous tissues (*3*, *4*). Spectral imaging quantifies variations in tissue oxygenation and melanin distribution. In contrast, polarization imaging reduces the superficial and specular reflectance from the air/tissue interface and enables higher visibility of the subsurface details (*4*). Combining these two modalities allows healthy tissues to be distinguished from diseased or damaged tissues with greater sensitivity than each measurement modality alone. Beyond channeled SPI approaches, which require thick birefringent elements for light modulation together with a spectrometer (*5*, *6*), current detector-level SPI strategies require temporal data collection (*7*) or snapshot imaging using spatially separated detection elements (*8*). The former is prone to temporal image misregistration, which severely degrades image quality. The latter resolves temporal misregistration but causes inherent spatial misregistration due to its four spatially separated polarization-sensitive detectors. This increases the size and cost of the image sensor and introduces spatial sampling errors, particularly around a scene's edges. Moreover, the spectral detection scheme in (*8*) is based on vertically stacked Silicon-based p-n junctions (*9*). This strategy exploits the spectrally dependent absorption coefficient of Si to distinguish color. However, the design is limited to three colors due to the strong attenuation of light in Si relative to the size of the subcell thickness, which inherently produces substantial color cross-talk (*10*). Alternatively, spectral detection by a single pixel can be achieved using vertically stacked organic photodetectors (*11*–*15*). Here, individual subcells are sensitive to different wavelengths of light through material selection, with the possible addition of spectral filters (*16*). However, relying on the absorption characteristics of a given organic heterojunction limits the ability to achieve narrowband detection and limits the number of spectral channels that can be sensed simultaneously. It also increases fabrication complexity due to the variations under material processing conditions needed for each material/color combination. To achieve simultaneous spectral and polarimetric sensing with a single pixel in a snapshot configuration, we introduce a bioinspired organic photodetector design that enables many of the same degrees of freedom found in the stomatopod's visual system.

The mantis shrimp (stomatopod)-inspired multispectral and polarization–sensitive (SIMPOL) sensor is achieved by combining intrinsically semitransparent polarization-sensitive organic photovoltaic (P-OPV) detectors with compact folded polymer retarders (FRs). Spectral detection is achieved using the FRs, together with panchromatic P-OPV cells, to form a Solc-like filter (*17*), enabling color selectivity through polarization interference. The use of polarization to control the spectral distribution of light, through a tandem detector structure, overcomes the spatial and temporal sampling errors of current SPI sensors (*7*, *8*) and enables light to efficiently transmit further into the tandem stack. Furthermore, because the light's spectrum is detected through polarization control, the incident polarization state can be easily measured. Last, the detector's subcells can be assembled with the same organic semiconductor active layer as it does not rely on the polymer's intrinsic spectral absorption properties to perform the spectral filtering, simplifying processing and fabrication. The design freedom of the SIMPOL sensor allows for broad control of the device's spectral and polarimetric sensitivity. The approach also highlights the unique

[1]Department of Electrical and Computer Engineering, North Carolina State University, 2410 Campus Shore Drive, Raleigh, NC 27695, USA. [2]Department of Mechanical and Aerospace Engineering and Organic and Carbon Electronics Laboratories (ORaCEL), North Carolina State University, 911 Oval Drive, Raleigh, NC 27695, USA. [3]Department of Chemistry, University of North Carolina at Chapel Hill, Chapel Hill, NC 27599, USA. [4]Department of Chemical and Biomolecular Engineering, Korea Advanced Institute of Science and Technology (KAIST), Daejeon 34141, Republic of Korea.
*Corresponding author. Email: btoconno@ncsu.edu (B.T.O); mwkudeno@ncsu.edu (M.K.)

attributes of polymer semiconductors that provide an advantage over their inorganic counterparts.

Here, we introduce the SIMPOL detector concept and demonstrate that it mimics the spectral and polarimetric modalities of the stomatopod visual system. We model the concept showing that it is capable of detecting 15 spectral bands over the visible spectrum. The P-OPV detector's fabrication approach is also provided, which was realized using a film-rubbing strategy applied to low–molecular weight (MW) all-polymer semiconductor active layers. This rubbing strategy increases the detectors' polarization sensitivity over previously reported P-OPVs, thereby improving system performance (*18*). Last, we experimentally demonstrate the concept with a sensor that consists of six tandem P-OPV detectors, in which the last four detectors alternate in series with four FRs to enable multispectral sensing. The different FR layers contain multiple thin polymer retarder films with optimized dispersion characteristics. This allowed a spectral resolution of up to 16.9-nm full width at half maximum (FWHM) with high spectral reconstruction accuracy, with an average root mean square error (RMSE) of 2.17%. In addition, the sensor can detect full linear polarization with an RMSE as low as 0.59%. All these features are obtained in what could be fabricated as a tandem 2D snapshot imaging array, showcasing the myriad degrees of freedom that P-OPV detectors offer in compact sensor design. To the best of our knowledge, the SIMPOL system marks the first detector design that can accurately mimic all of the degrees of freedom found in the mantis shrimp's visual system, with the advantage that both multispectral and polarization sensing are achieved simultaneously along the same optical axis. This concept provides a route to vastly improve hyperspectral and polarization imaging over the current state of the art.

A biological parallel

The SIMPOL sensor concept was inspired by the degrees of freedom present in the stomatopod visual system. The compound eye of mantis shrimp contains spectrally selective and polarization-sensitive elements that are vertically stacked along a single optical axis. As light propagates into the stack, the mantis shrimp extracts spectral and polarization information. Analogously, the SIMPOL sensor comprises spectrally selective (the FRs) and polarization-sensitive elements (the OPVs) that are vertically stacked along a single optical axis. The spectral and polarization information is detected in a similar manner as the mantis shrimp's eye, enabling simultaneous hyperspectral and polarimetric detection. To shed more light on the specifics of the two systems, we first introduce the light detection concept of the mantis shrimp, followed by the SIMPOL sensor.

A stomatopod (*Odontodactylus scyllarus*) is pictured in Fig. 1A with an illustration of an anterior view of the apposition eye given in Fig. 1B. The stomatopod eye consists of tens of thousands of optical units known as ommatidia, which form three sections: the ventral hemisphere (VH), dorsal hemisphere (DH), and a narrow midband (MB) (*19*). As depicted in Fig. 1D, the MB layer is characterized by six distinct rows of specialized ommatidia. Rows 1 to 4 contain up to 12 photoreceptors, with spectral sensitivity ranging from the ultraviolet (UV) to the far-red (*20*–*22*), while rows 5 and 6 are sensitive to circular polarization (*23*). Light first enters the cornea and crystalline cone, which focuses it into a receptor region called the rhabdom. Here, light is chromatically filtered through pigmented cells and traverses a series of photosensitive retinular cells (R8 and R1 to R7) that are vertically stacked in the rhabdom. A bidirectional cross section of the retinular cells of stomatopods is depicted in Fig. 1C. These cells, specifically in the VH and DH regions, feature orthogonally arranged interdigitating microvilli, which collectively serve as polarization analyzers (*24*). Across the whole eye, the rhabdom orientations in the VH are offset by 45° compared to those in the DH, yielding four unique microvillar orientations, as depicted in the bottom part of Fig. 1D. Comparisons between these four orientations exist at the neural level, enabling the reconstruction of partially linearly polarized light. Note that these spectral and polarization modalities cannot be all realized in a single ommatidium (pixel) of the mantis shrimp but rather across multiple ommatidia.

The SIMPOL detector accommodates many features of the mantis shrimp's eye, with the advantage that all the optical modalities (spectral and polarization) are simultaneously realized in a single pixel. An example SIMPOL sensor is depicted in Fig. 1E. It consists of six semitransparent P-OPVs (OPV1 to OPV6) and a linear polarizer (LP) placed beneath OPV2 in the stack. In addition, OPV3 through OPV6 sequentially alternates with birefringent folded retarders FR1 to FR4. Each FR consists of N layers of polymer retarder films (r_1 to r_N), with equal thicknesses L and fast axes oriented in a folded manner, i.e., alternating between an angle of $\pm\theta$, as illustrated in Fig. 1F. The polarization sensitivity of the OPV cells can then be introduced by orienting the polymer semiconductors in the plane of the film and exploiting the anisotropic optical character of the polymers (*25*–*27*). Referring to Fig. 1E, OPV1 and OPV2 sense polarization, while OPV3 to OPV6 sense color and also provide a single polarization channel. The light's polarization state is detected by OPV1 and OPV2, which are nominally sensitive to 0° and +45° polarized light relative to the x axis, respectively. While these detectors absorb light across a wide range of wavelengths, optimizing their diattenuation and transmittance enables most of the light to enter the spectral sensor (OPV3 to OPV6), offering a reasonable trade-off between the polarimetric and spectral signal-to-noise ratios. The transmitted light at the output of OPV2 is then polarized by a LP (LP0), with a transmission axis parallel to the x axis. The light then traverses the first birefringent element FR1 and experiences successive phase retardations from a series of retarder layers r_1 to r_N. This process results in spectrally dependent polarization rotations. The light's polarization state for in-band light is rotated by 90°, enabling OPV3 to absorb it, while out-of-band light undergoes no rotation, enabling OPV3 to transmit it to subsequent OPV detectors. The transmitted light can be further rotated and detected by subsequent FRs and OPVs. Additional examples, illustrating the chromatic polarization rotation and tandem color detection concepts, are provided in figs. S1 and S2, respectively. With proper tuning of the OPVs' transmittances and the folded retarders' parameters, arbitrary OPV absorption profiles with specific finesse, free spectral range, and sidelobe levels can be obtained (*17*). In addition, because all spectral OPVs (OPV3 to OPV6) have absorption axis perpendicular to the x axis, their spectral integral provides a third spectrally broadband polarization channel that yields a nominal measurement of +90° polarized light. Combined with the information obtained from OPV1 to OPV2, our SIMPOL sensor enables broadband full linear polarimetry and multispectral sensing, which are realized simultaneously on a single pixel.

The functional similarities of our sensor to the visual system of the mantis shrimp lie in four main aspects: (i) The conjugated polymer chains are analogous to the microvilli found in the rhabdom; (ii) the folded retarders are analogous to the pigmented cells; (iii) OPV1

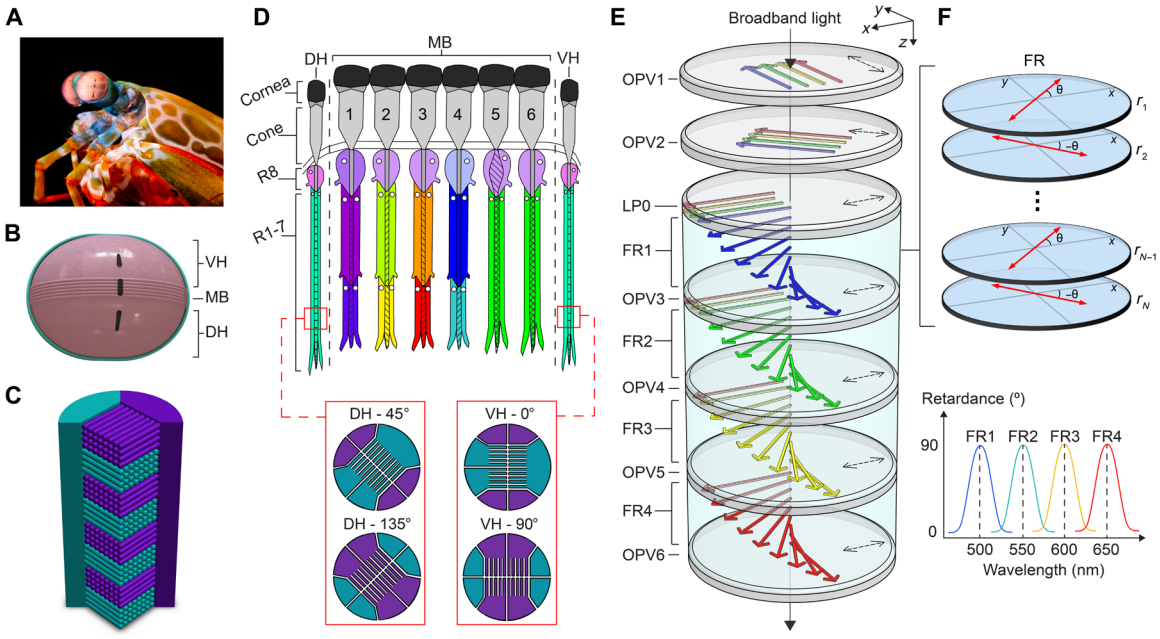

Fig. 1. Mantis shrimp eye and bioinspired detector. (**A**) Image of a mantis shrimp (*O. Scyllarus*). Photo credit: Michael Bok, Lund University. Representations of (**B**) the frontal view of the stomatopods eye, (**C**) bidirectional cross section of the rhabdom, (**D**) sagittal cross section of the midband (*24*, *57*). Cells R1 to R8 are colored differently to distinguish their spectral sensitivity. (**E**) The structure of the SIMPOL sensor. Dashed arrows indicate the diattenuator's transmission axis. (**F**) The folded retarder elements and the designed spectral retardance of each folded retarder.

to OPV6 are analogous to the photoreceptor cells; and (iv) the SIMPOL stack is aligned along a single optical axis, which can be compared to a single ommatidium stack. All these features can be realized in a single-pixel sensor structure. Last, the number of spectral channels is primarily limited by the OPV's transmittance and responsivity properties. For OPVs with near-ideal diattenuation, in combination with aligned liquid crystal films (*28*), our concept can be readily expanded to hyperspectral sensing and full Stokes polarimetry.

RESULTS AND DISCUSSION

Theoretical system model

The mathematical representation of the system is derived using Mueller calculus with details of the model provided in the Supplementary Materials. Referring to Fig. 1E, we consider a broadband light source at the input of the first OPV cell. In addition, we modeled each OPV cell as a nonideal diattenuator. The component of the electric field that is parallel to the aligned polymer semiconductors in the OPV cells is maximally absorbed, whereas that which is perpendicular to the OPV's molecular alignment axis is maximally transmitted. The method to obtain full linear polarimetry is similar to that described in our previous work (*29*). As depicted in Fig. 1E, the intensities obtained from OPV1 and OPV2 represent 0° and 45° polarization channels, respectively. The 90° polarization channel can be obtained by adding up the individual intensities from OPV3 to OPV6. From the absorption of light by each cell, one can determine the linear Stokes parameters, which characterize the polarization state of light. However, because of the nonideal polarization characteristics of a P-OPV and the tandem nature of the structure, the Stokes parameters incur errors in reconstruction. To fully reconstruct the Stokes parameters with high accuracy, we apply a data reduction matrix (DRM) method previously described (*30*).

The spectral detection is captured by tracing the polarization orientation of the spectrally dependent polarized light incident on each OPV cell in the stack. On the basis of this, we quantified the spectral performance of the SIMPOL system depicted in Fig. 1E, considering nonideal P-OPV cells, with absorptance (A) of $Ay = 0.8$ and $Ax = 0.1$. The polymer retarder films are modeled using the birefringence data of polycarbonate, with $N = 4$ and $\theta = \pi/4N$. In addition, we simulated the retarders' thicknesses for FR1 to FR4 to be 111.75, 134, 156, and 186.2 μm, respectively. This resulted in peak spectral sensitivities of 475, 547.5, 614, and 696 nm. Figure S3 depicts the simulated individual transmission spectra for FR1 to FR4, when placed between two crossed ideal polarizers. Notice that FR4 produced a higher-order spectral transmission mode in addition to the first-order mode. Here, the first-order spectral transmission mode corresponds to a retardance of 1.5 waves, whereas the second-order mode corresponds to a retardance of 2.5 waves. We designed FR1 to have peak spectral sensitivity that overlaps with the higher-order mode of FR4. In this way, the cross-talk is naturally rejected as the light propagates through the different layers, similar to a Lyot filter (*31*). Figure 2A displays the absorption spectra for the nonideal P-OPV cells. Under these conditions, the magnitude of the OPVs' absorption profile decreases as light transmits through the stack. OPVs with optimized vertical absorptance can counteract this behavior to normalize the detectors' responses, with details provided in table S1 and fig. S4. In addition, it can be noted from Fig. 2A that the FWHMs are 49 and 58 nm for OPV3 and OPV6, respectively, while OPV4 and OPV5 have values between this range. The FWHM can be reduced with an increase in the number of retarder films (N) used in the FRs. This effect is depicted in Fig. 2B, where it is found that the spectral resolution with $N = 10$ is lowered to 12 nm. Improving the spectral resolution allows more spectral channels to fit within a specific spectral bandwidth. We demonstrate this by considering

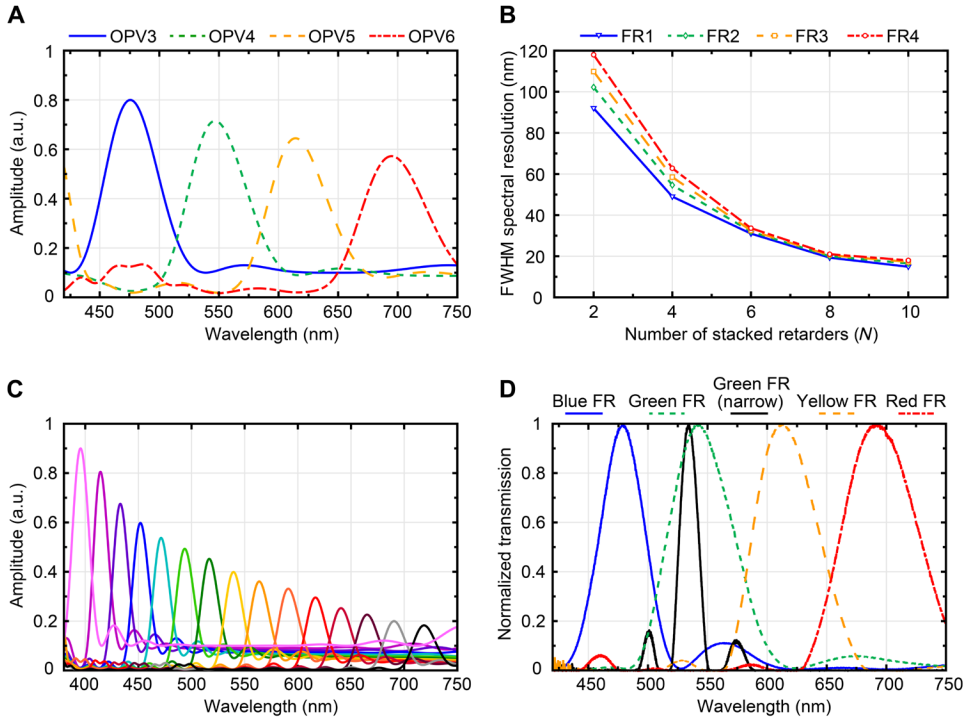

Fig. 2. Spectral sensitivity of the detector. (**A**) The modeled absorption spectra for four stacked OPV-FR pairs with nonideal OPV dichroism. a.u., arbitrary units. (**B**) The FWHM spectral resolution as a function of the number of retarders for each folded retarder. (**C**) The modeled absorption spectra for 15 stacked OPV-FR pairs with near-ideal OPV dichroism. (**D**) The measured transmission spectra of the fabricated FR filters.

a SIMPOL sensor design that consists of 15 stacked FR-OPV pairs. In this case, we assumed that the P-OPV detectors have near-ideal dichroism of $Ay = 0.9$ and $Ax = 0.1$. In addition, the FRs are modeled with $N = 10$. The simulation result is displayed in Fig. 2C showing sensitivity to an average spectral resolution of 17 nm over a spectral range of 380 to 750 nm. These results underscore the potential of our SIMPOL sensor to achieve hyperspectral imaging. This capability is particularly beneficial for applications that require the acquisition of narrowband spectral images to reveal distinct features of the sample under test (*3*, *4*).

SIMPOL detector characterization

Before considering the SIMPOL sensor spectral and polarimetric imaging capabilities, we experimentally characterize the critical components of the device, namely, the FRs and P-OPVs. We fabricated five distinct folded Solc filters using a blend of different polymer retarder films with details provided in Materials and Methods and the design parameters provided in tables S2 and S3. The fabricated FRs enabled necessary polarization control to demonstrate the concept within a relatively thick (several millimeters) structure; however, much thinner (microns) retarders can be fabricated using aligned liquid crystal films within multitwist retarders, providing a path forward for thinner compact designs (*28*, *32*). The FR filters were characterized using the experimental setup depicted in fig. S5, where the transmission response of each FR filter was independently measured. Figure 2D provides the experimental results of the transmission spectra for the four broad filters ($N = 4$) and the narrow green filter ($N = 10$). Each filter's transmission response was normalized to its peak value. Note that the sidelobe levels of the narrow green filter are not balanced. This is likely caused by small fast axis misalignments between the polymer films. To quantify the accuracy of our fabrication process, we measured the RMSE of the four broad filters in Fig. 2D when compared to those simulated in fig. S3. The RMSE was calculated across a spectral bandwidth of ±50 nm from the center wavelength of each FR filter. The RMSE for the blue, green, yellow, and red filters were 9.2, 1.2, 5.6, and 3.4%, respectively. Last, the spectral resolution of the narrow green filter in Fig. 2D was only 16.9 nm, which demonstrated the efficacy of using polarization control to achieve a narrowband spectral profile.

The intrinsic P-OPV cells were realized through orienting the active polymer semiconductors in the plane of the film, as previously described (*25*, *27*, *33*, *34*). This exploits the optical anisotropy of the polymers, which have their primary optical transition dipole moment (π-π^*) aligned parallel to their backbone (*35*, *36*). We have previously demonstrated an alignment technique using uniaxial strain on the active layer to fabricate polarization-sensitive detectors (*25*, *29*, *37*). This includes the strain alignment of an all-polymer semiconductor bulk heterojunction (BHJ) active layer with polymers PBnDT-FTAZ and P(NDI2OD-T2). The chemical structure of these two polymers is depicted in Fig. 3A. These polymers were chosen because they are both ductile at room temperature and have complimentary spectral absorption, enabling panchromatic P-OPV cells (*27*, *38*). However, the strain alignment approach limited the peak dichroic ratios to approximately 2 at the maximum possible strain before film tearing (*27*). To achieve higher dichroic ratios that assist in reducing the detectors' optical cross-talk, we oriented the polymer semiconductor active layer through a rubbing process. Mechanical rubbing is a highly effective postprocessing alignment strategy for neat conjugated polymer films (*18*, *39*–*41*). This has been shown to work particularly well for lower MW polymers. Here, we extend the process

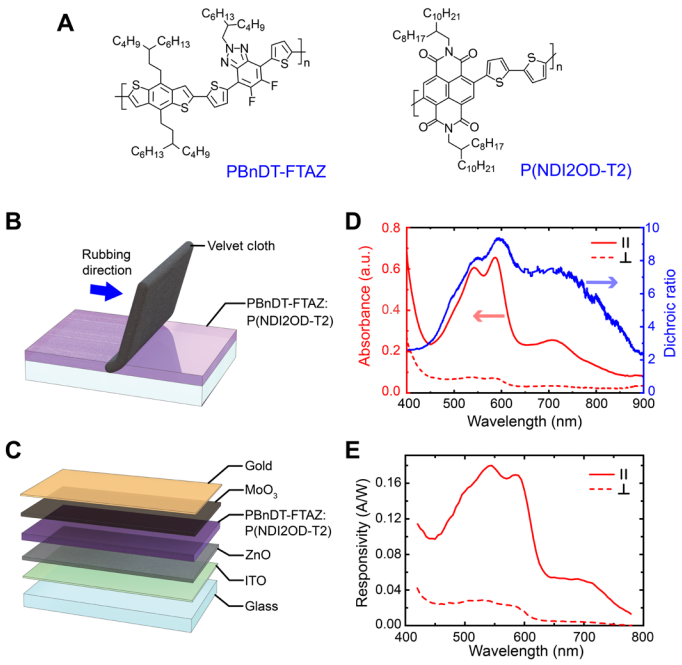

Fig. 3. Organic photovoltaic details. (**A**) Chemical structure of PBnDT-FTAZ and P(NDI2OD-T2). (**B**) An illustration of the rubbing procedure to orient the polymer semiconductor layer and (**C**) the layers of the semitransparent polarized OPV cell. (**D**) The absorbance anisotropy of the oriented PBnDT-FTAZ: P(NDI2OD-T2) film under linearly polarized light parallel (∥) and perpendicular (⊥) to the rubbing direction, and the resulting dichroic ratio. (**E**) Responsivity of P-OPV cell under linearly polarized light ∥ and ⊥ to the rubbing direction under 0-V bias.

to the PBnDT-FTAZ:P(NDI2OD-T2) BHJ layer. The solution-cast films were physically rubbed at elevated temperatures to orient the polymer chains in the plane of the film, as illustrated in Fig. 3B. We used low MW PBnDT-FTAZ and P(NDI2OD-T2) to maximize alignment and achieve dichroic ratios over 9, as shown in Fig. 3D. The aligned polymer film was then layered between semitransparent electrodes made from indium tin oxide (ITO) and a 10-nm gold film. A schematic of the device stack is presented in Fig. 3C along with the responsivity of the OPV cell, depicted in Fig. 3E. The current-voltage characteristics of a typical P-OPV cell under white light illumination, together with its optical transmittance, are also provided in fig. S6. As shown in fig. S6 (A and B), the dark current of the devices was below 10^{-5} mA/cm^2 under −0.5-V bias, similar to other polymer-based photodetectors (*27*, *42*–*44*). The devices exhibited good current-voltage characteristics while showing no major device degradation associated with the rubbing process, such as reduced shunt resistance. Moreover, as depicted in fig. S6C, the devices displayed a transmittance of approximately 80% at 600 nm for light polarized perpendicular to the oriented polymer layer highlighting a key advantage of this approach. Note that the primary goal was to realize multipurpose OPV cells to serve the SIMPOL sensor's requirements and accentuate its features. Thus, they were optimized to provide a balanced design tradespace regarding dichroic ratio, responsivity, spectral bandwidth, and transmittance. In terms of these metrics, the demonstrated polymer-based detectors outperform other intrinsically polarization-sensitive detectors recently reported (*45*–*47*).

Polarization and spectral imaging

We experimentally performed spectral and polarization imaging using a single-pixel SIMPOL sensor. The imaging technique adopted here was to spatially raster scan across the target, while our SIMPOL sensor remained stationary. The complete experimental setup is depicted in Fig. 4A and fig. S7. The sensor structure consisted of six OPV detectors (OPV1 to OPV6) and four FR filters (FR1 to FR4). The OPV polarization axes were oriented, as illustrated in Fig. 1E. With respect to the *x* axis, OPV1 was oriented at 0°, OPV2 was oriented at 45°, and OPV3 to OPV6 were oriented at 90°. In addition, the red, blue, green, and yellow FR filters were placed in front of OPV3, OPV4, OPV5, and OPV6, respectively. This configuration enabled four spectral channels to be detected using OPV3 to OPV6 along with three panchromatic polarization intensities using OPV1 (I_0), OPV2 (I_1), and a summation of the detected intensities from OPV3 to OPV6 (I_2). This provides three intensities I_0, I_1, and I_2 that are nominally equivalent to I_0, I_{45}, and I_{90} in polarimetry; however, given the tandem nature of the structure, more sophisticated data reduction techniques were applied (*29*, *37*).

The target chosen in the experiment was an image consisting of seven colored pencils printed on transparency film, as depicted in Fig. 4A. The image size was 47 mm by 47 mm. We also added polarization features to the image by cutting an LP film to denote NCSU, with each letter containing a different polarization angle. We experimentally measured each letters' polarization angle using a rotating polarization analyzer and a radiometer. For each letter, we rotated the reference analyzer until the output of the radiometer returned a minimum intensity value, indicating a 90° offset between the letter and the reference analyzer. The polarization angles of each letter were measured to be 5°, 166°, 99°, and 142° for N, C, S, and U, respectively. The same reference polarizer and method were used to determine the transmission axes of the OPV cells to establish a common reference frame.

The polarization imaging results are shown in Fig. 4 (B to G) and fig. S8. The reconstructed S_1/S_0 and S_2/S_0 images, depicted in Fig. 4 (C and D), were obtained after performing polarimetric calibration on the raw OPV images in fig. S8. A spatial RMSE calculation was performed across each letter independently, relative to its theoretical Stokes parameter. Table 1 summarizes the RMSE results for each letter. The RMSE results in Table 1 demonstrate that the adopted DRM calibration method yielded low reconstruction errors for the Stokes parameters S_1/S_0 and S_2/S_0, with the largest RMSE being 2.51%. In addition, the average RMSEs for S_1 and S_2 across the four letters were calculated to be 1.35 and 1.19%, respectively. Figure 4 (B, E, and F) depicts the light's total intensity S_0, the degree of linear polarization (DoLP), and the angle of polarization (AoP), respectively. Figure 4H depicts a color fusion image based on adapting the hue-saturation-value polarization-color mapping, with a perceptually uniform colormap "Viridis," as previously described (*48*). In this color representation scheme, the values of AoP, DoLP, and S_0 were mapped to hue, saturation, and value, respectively. The measured polarization angles of the four letters showed good agreement with the theoretical polarization angles given in Table 1.

In addition to the polarimetric imaging results, we simultaneously acquired four unique spectral images from OPV3 to OPV6. The results are depicted in Fig. 5 (A to D). Each FR-OPV pair displayed high brightness for those pencils, whose spectral response overlapped with the FR's spectral response. Conversely, darker pencil regions indicated that the pencils' spectral response was not coinciding

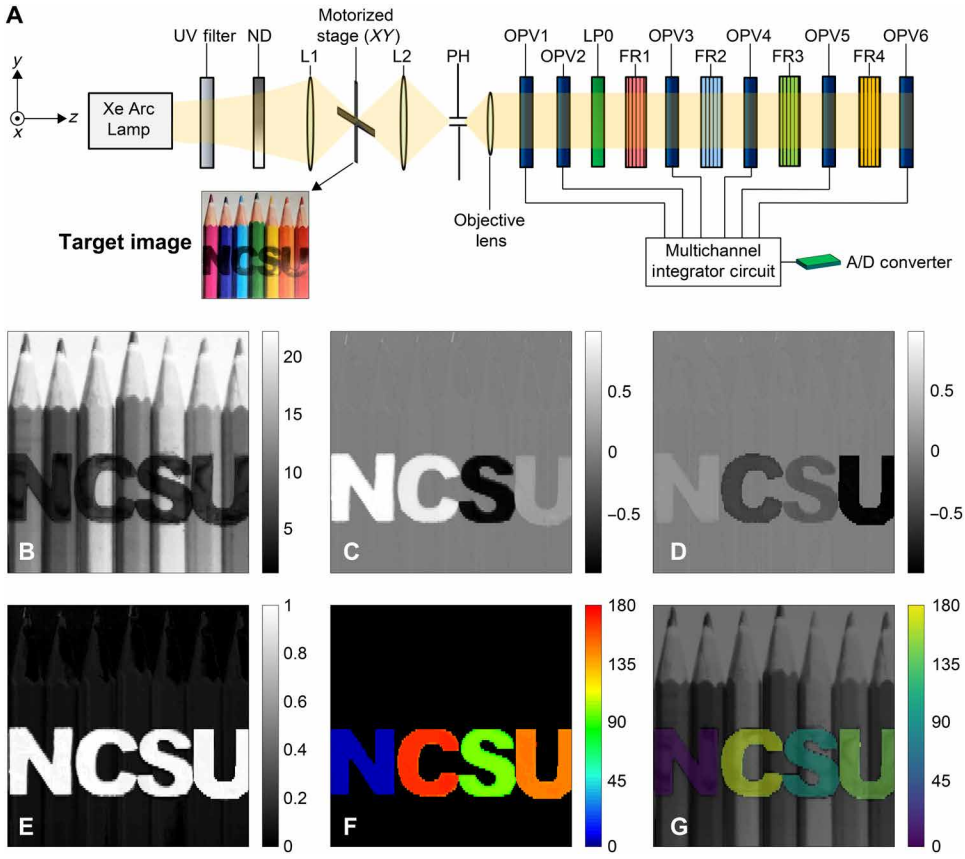

Fig. 4. SIMPOL imaging setup and polarization imaging. (**A**) Experimental setup of the SIMPOL single-pixel camera, (**B**) total intensity S_0, (**C**) S_1/S_0 reconstruction, (**D**) S_2/S_0 reconstruction, (**E**) DoLP, (**F**) AoP, and (**G**) perceptually uniform polarization-color mapping Viridis. Photo credit of target image: Colin, CC-BY-SA-4.0 (*58*). ND, neutral density filter; PH, pinhole.

Table 1. RMS errors of the reconstructed Stokes images.

Letter	Polarization angle (°)	$\frac{S_1}{S_0}$ theory	$\frac{S_2}{S_0}$ theory	$\frac{S_1}{S_0}$ RMSE (%)	$\frac{S_2}{S_0}$ RMSE (%)
N	5	0.985	0.17	0.71	0.59
C	166	0.883	−0.47	2.09	0.94
S	99	−0.951	−0.31	1.47	0.73
U	142	0.242	−0.97	1.14	2.51

with or close to the FR's response. For example, for the OPV4 image, it can be seen that the cyan pencil displayed higher brightness relative to other pencils, indicating that its spectrum coincided with the center wavelength of the blue FR filter of 487 nm. Moreover, we combined the four spectral channels in Fig. 5 (A to D) to form a color composite image of the target, as shown in Fig. 5E. The technique adopted here was based on the true color composite scheme with a correlation coefficient metric associated with each spectral band as previously described (*49*).

We have also validated the spectral response of OPV3 to OPV6. Equation S22 was used to reconstruct each pencils' transmission spectrum, which was then compared to a reference measurement taken with a UV-visible (UV-Vis) spectrometer. The reconstructed pencils' transmittances are given in Fig. 5 (G and H). For comparison, we have also displayed the known measured transmittances of the seven colored pencils. RMSE calculations were performed for the reconstructed pencils' transmittances relative to their known measured values. The RMSE results are provided in Fig. 5 (G and H). The spectral reconstruction errors were all below 3%. These results indicate that the spectral calibration method, adopted for the SIMPOL sensor, provides accurate spectral reconstruction. Last, we combined the SIMPOL polarization images with the color composite image to demonstrate the simultaneous information that the sensor can provide, as depicted in Fig. 5F. The polarization's magnitudes and orientations are represented as vector fields (white arrows), where the arrows' length and orientation denote the DoLP and AoP, respectively.

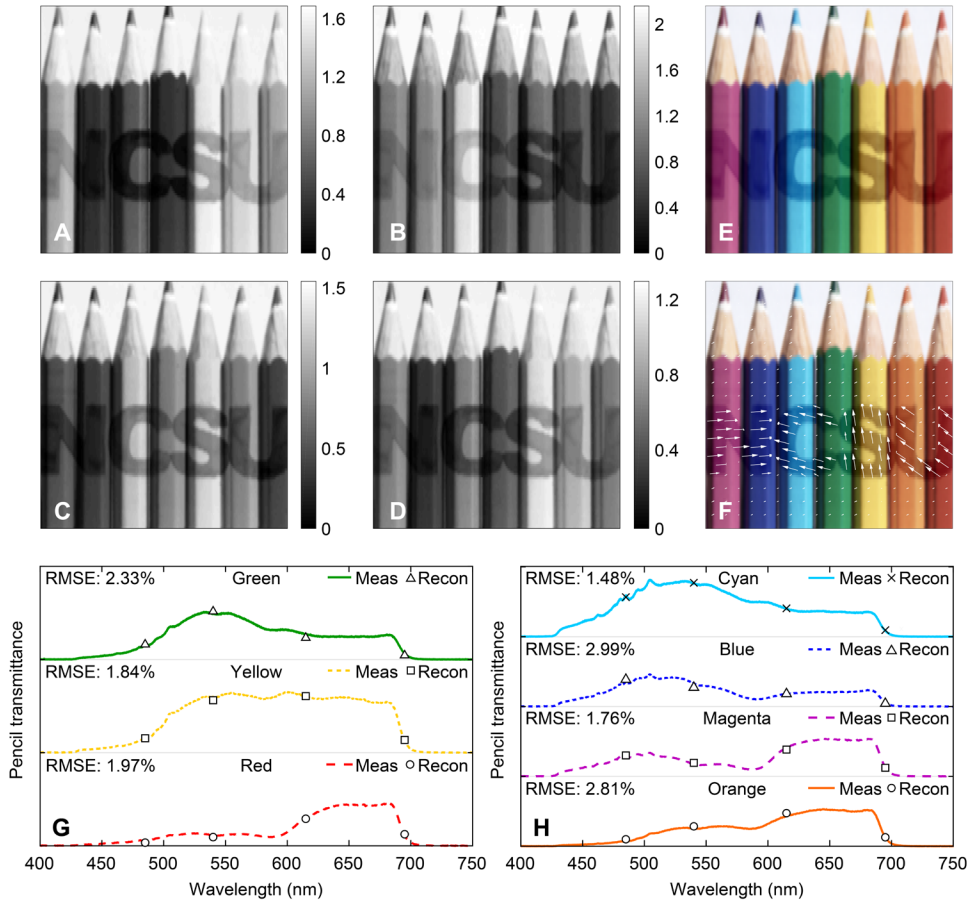

Fig. 5. Combined spectral and polarization imaging. Spectral images from (**A**) OPV3, (**B**) OPV4, (**C**) OPV5, and (**D**) OPV6. (**E**) Color composite from the OPV detectors and (**F**) color image combined with polarization image where polarization is represented by the arrows. The measured and SIMPOL reconstruction of the pencils spectra for (**G**) green, yellow, and red pencils and (**H**) cyan, blue, magenta, and orange pencils. Photo credit of target image: Colin, CC-BY-SA-4.0 (*58*).

While we have successfully demonstrated the full capabilities of the SIMPOL sensor in a free-space configuration, future directions involve (i) monolithically integrating the SIMPOL sensor in a compact design and (ii) realizing a pixelated 2D array of the SIMPOL sensor for real-time imaging. A key advantage of the SIMPOL sensor is that the OPV layers are fabricated from the same material, with uniform optical and electrical properties. In addition, the folded retarders can be made from liquid crystal polymers, which are thinner than standard polymer retarder films by two orders of magnitude while preserving the color filtering performance (*32*). These two factors substantially facilitate the fabrication of a single SIMPOL pixel, enabling a roll-to-roll process on a single substrate, using, e.g., soft lithographic techniques (*50*, *51*). These developments may enable a monolithic SIMPOL sensor with a total thickness on the order of microns. The rubbing process to align the active layer should also be scalable as each OPV layer would consist of a rubbed film in the same orientation and there would be no need for a different film alignment at neighboring pixels. Thus, blank film alignment could be achieved, followed by patterning to isolate the detector elements (*52*). A final important step would be extending the single SIMPOL pixel to a pixelated 2D array. To this end, a promising solution is to use complimentary metal-oxide semiconductor–based organic image sensors, which have previously showcased high performance imaging capabilities (*53*, *54*). Because of these factors, we believe that the realization of a monolithic SIMPOL sensor array is achievable, especially considering the advanced fabrication techniques developed for commercial organic light-emitting diode displays.

In conclusion, a bioinspired spectropolarimetric sensor referred to as a SIMPOL sensor, which can mimic the visual system of the mantis shrimp, has been presented. The structure is based on integrating P-OPVs with polymer retarders to enable remarkable degrees of freedom in multispectral and polarization sensing. Modeling shows that this design approach is capable of measuring over 15 spectral channels from 400 to 750 nm. Experimentally, we demonstrate that our bioinspired sensor can detect four spectral channels, with a spectral resolution of up to 16.9-nm FWHM, and can provide high spectral reconstruction accuracy, with an average RMSE of 2.17%. In addition, the sensor can detect three polarization channels and perform polarimetric reconstructions with an RMSE as low as 0.59%. This sensor has the potential to make a considerable impact on the use of organic semiconductors as photodetectors, motivating the development of compact monolithic organic detectors capable of hyperspectral and polarization imaging along a single optical axis. The SIMPOL detector will be particularly beneficial in imaging applications that require simultaneous measurements of the spectral and polarimetric data and necessitate small sensor size, yet with efficient polarization and spectral performances.

MATERIALS AND METHODS

Custom Solc filter design and fabrication

Five distinct Solc filters were fabricated using different polymer retarder films from American Polarizers Inc. The specifications of these films are provided in table S2. Instead of optimizing the films' thickness, we relied on combining different types of wave plates to produce the desired dispersion curve. Table S3 provides the design parameters and methods for making the five Solc filters. Note that the "retarder unit" in table S3 is equivalent to a single retarder film (r) illustrated previously in Fig. 1F. Each retarder unit consisted of different films with fast axes aligned in the same direction. However, from one retarder unit to another, the fast axes were aligned in a folded manner with azimuth angles ±θ. For example, the blue FR was made up of four retarder units, in which the first and the third were oriented at +11.25°, whereas the second and the fourth were oriented at −11.25°. The process of cutting the retarder films to the desired azimuth angle was achieved using a high precision digital T-bevel with a resolution of 0.05°. The films were then glued on top of each other using Norland optical adhesive 61 and were lastly exposed to UV light for the polymer curing process. Before incorporating these FRs into the OPV-based sensor, we examined their performance by placing one FR at a time between two crossed polarizers to form a Solc filter. A tungsten lamp, with a broadband spectrum from 420 to 800 nm, was then used as the optical source, and a spectrometer was placed at the output of the system to detect the transmitted spectrum. Figure S5 shows the experimental setup.

Polarized-OPV design and fabrication

The active layer consisted of a PBnDT-FTAZ with the number-average MW (M_n) of 40.9 kDa and dispersity ($Đ$) of 1.96 and P(NDI2OD-T2) with an M_n of 20 kDa and a dispersity of 1.5. The polymers were dissolved in chlorobenzene at 12 mg/ml at a 1:1 ratio by weight. Both materials were synthesized through previously described methods (*38*). The solution was then cast onto a cleaned glass substrate at 2000 rpm to obtain a film of approximately 40 nm. The sample was placed on a hot plate held at 160°C. After 2 min, the film was physically rubbed with a velvet cloth for 80 cycles. After the rubbing process, the film was exposed to a postanneal at 250°C for 5 min, which further increased the degree of chain alignment. The postrubbing annealing step was performed in a nitrogen-filled glovebox. The absorbance spectrum of these films was measured using an UV-Vis spectrometer, revealing a peak dichroic ratio of ~9.5 at 595 nm with values above 6 for a majority of the visible spectrum.

The oriented polymer blend films were then incorporated into semitransparent OPV devices. The fabrication of the devices began by patterning ITO-coated glass substrates using a previously described photolithography technique (*55*). The patterned ITO substrates were cleaned, followed by spin-casting ZnO nanoparticles at 6000 rpm for 50 s in ambient air. The films were dried by thermally annealing at 120°C for 10 min. The substrates were then brought into a nitrogen-filled glove box where the PBnDT-FTAZ:P(NDI2OD-T2) solution was spun cast. The films were then rubbed following the procedure outlined above. The device fabrication was completed by depositing a 20-nm MoO_3 hole-transport layer and a 10-nm gold electrode by vacuum thermal evaporation. The relatively thick MoO_3 layer was applied to help reduce shunting that may arise because of the rubbing process. The current-voltage characteristics of the detector (measured area of 0.25 cm^2) were obtained by exposing the devices to polarized light parallel and perpendicular to the direction of alignment, with results given in fig. S6 (A and B). A large photocurrent anisotropy was observed for these devices with a short circuit current ratio over 5, which is over three times greater than our previous polarization-sensitive organic diode demonstration (*27*). Moreover, measurements of the OPV's transmittance, for incident light polarized parallel and perpendicular to the OPV's absorption axis, are provided in fig. S6C.

Spectral characterization of the SIMPOL detectors

The multispectral detector experimental setup is depicted in fig. S9A. The detector consisted of fourfolded retarders (FR1 to FR4) alternating in series with four semitransparent P-OPVs (OPV3 to OPV6), with transmission axes oriented along the x axis. Among our five fabricated FRs per Fig. 2D, we incorporated the red (FR1), blue (FR2), narrowband green (FR3), and yellow (FR4) into the experimental setup. Note that the reason we placed the red filter first was due to the lower responsivity of the OPV beyond 650 nm. An LP was placed in front of the multispectral detector, with the transmission axis oriented along the x axis. The light source was a Xenon arc discharge lamp (XBO 75, OSRAM), followed by a monochromator (MicroHR, HORIBA) to scan the incident light from 420 to 680 nm in 5-nm increments. The normalized intensities, as measured by the OPV cells, are provided in fig. S9B. These measurements were obtained by converting the OPVs' photocurrent to light intensity using the responsivity of the devices, with details provided in Materials and Methods. The absorption spectra of the four tandem OPVs closely follow the independently measured spectra given in Fig. 2D. Notable differences include a reduced contrast, caused by the OPV's nonideal diattenuation, as well as a tapering amplitude, caused by the nonideal transmission of the OPV's electrodes and the high transmission axis of the OPV cells. One exception is OPV3, which produced a lower amplitude compared to other OPV cells due to the low OPV responsivity beyond 620 nm.

Designs of the SIMPOL experiment

In the SIMPOL experimental setup as illustrated in fig. S7, two lenses (L1 and L2) were used, both having a focal length of 50 mm and a numerical aperture of 0.25. The first lens (L1) was used to focus light onto a specific point on the target image and was located 5 cm away from the target. The second lens (L2) was used to relay a point source from the target to a pinhole. In addition, L2 was placed 10 cm behind the target and 10 cm away from the pinhole to provide a 1:1 magnification ratio. The pinhole was used to spatially filter the target's point spread function. The size of the pinhole was chosen to be 300 μm to allow sufficient light to reach the last detector in the stack, while simultaneously enabling reasonable spatial resolution for the detected image. A microscope objective, with a magnification of 4 and a numerical aperture of 0.1, was placed after the pinhole to magnify and collimate the light at the input of the SIMPOL sensor. The target image was then mounted on a motorized translation stage (KMTS50E, Thorlabs Inc.), which was programmed and automated using LabVIEW to form a 228 pixel by 112 pixel image.

Method for measuring the OPVs' absorptances

To measure the spectral absorption profile of OPV3 to OPV6, as shown in Fig. 4B, we used a low noise, charge integrator chip (ACF2101, Burr-Brown) with an integration time (t_{int}) set at 16.67 ms and a feedback capacitance (C_{int}) of 100 pF. This circuit converted the

photocurrents produced from OPV3 to OPV6 to voltages. We then measured and recorded the OPV voltages using a multifunction instrument (Analog Discovery 2 from Digilent). The steps to obtain the measured normalized intensity were as follows:

1) We removed the dark voltages (OPV voltages measured in the dark) from all measured OPV voltages.

2) We then converted all OPV voltages (V_{OPV}) to photocurrents (i_{OPV}) using the integration time and feedback capacitance of the integrator circuit.

$$i_{OPV} = \frac{C_{int}}{t_{int}} V_{OPV}$$

3) We converted all OPV photocurrents to intensities using the OPV responsivity data provided in Fig. 3E.

4) We normalized the results to the intensities incident on the OPV for all wavelengths.

Method for image acquisition

To measure all the spectral and polarization images simultaneously, we have built an eight-channel integrator circuit, which consisted of 4× ACF2101 chips. The voltage outputs from the eight channels were multiplexed and sent to an analog-to-digital (A/D) converter, which selected and recorded each output. In addition, the multiplexer circuit was built with the option to add an external feedback capacitance of 910 or 10,000 pF in parallel with the ACF2101's internal capacitance of 100 pF. These capacitors enabled a factor of 1, 10, or 100 in dynamic range to be used for each OPV detector. A trigger port was also added to the integrator circuit and was connected to a stepper motor. This port enabled the stepper motor to trigger the A/D converter circuit to record data whenever the target was moved to the next pixel.

For all measurements, the integrating capacitance of OPV1 and OPV2 was 1010 pF, while that of OPV3 to OPV6 was 100 pF. OPVs' voltage offsets, produced from the OPV dark currents, were also removed from all measurements. The image scanning range was 45.6 and 44.8 mm in the x and y direction, respectively, with spatial sampling in x and y of $\Delta x = 0.2$ mm and $\Delta y = 0.4$ mm, respectively.

SIMPOL calibration

Before performing spectral and polarization imaging, we built and calibrated the SIMPOL system illustrated in Fig. 1E. The polarization calibration method was based on the DRM technique, described by Lu and Chipman (*56*) where the coefficients of a measurement matrix were fitted to measure OPV voltages measured under known polarization states (fig. S10). Meanwhile, the spectral calibration process focused on mapping the absolute transmission of the sample mounted in the system to the voltages measured from OPV3 to OPV6. The detectors were calibrated using four different dye-based color filters (Roscolux) with known transmittances (fig. S11). Filters were selected to provide high modulation rates within the four spectral channels defined by the FRs. Filters included red (#26), orange (#23), green (#86), and blue (#376). The polarimetric and spectral calibration steps are documented in the Supplementary Materials.

SUPPLEMENTARY MATERIALS

Supplementary material for this article is available at http://advances.sciencemag.org/cgi/content/full/7/10/eabe3196/DC1

REFERENCES AND NOTES

1. J. S. Tyo, D. L. Goldstein, D. B. Chenault, J. A. Shaw, Review of passive imaging polarimetry for remote sensing applications. *Appl. Optics* **45**, 5453–5469 (2006).
2. Y. Zhao, C. Yi, S. G. Kong, Q. Pan, Y. Cheng, *Multi-Band Polarization Imaging and Applications* (Advances in Computer Vision and Pattern Recognition, Springer Berlin Heidelberg, 2016).
3. Y. Pu, W. B. Wang, G. C. Tang, F. Zeng, S. Achilefu, J. H. Vitenson, I. Sawczuk, S. Peters, J. M. Lombardo, R. R. Alfano, Spectral polarization imaging of human prostate cancer tissue using a near-infrared receptor-targeted contrast agent. *Technol. Cancer Res. Treat.* **4**, 429–436 (2005).
4. F. Vasefi, N. MacKinnon, R. B. Saager, A. J. Durkin, R. Chave, E. H. Lindsley, D. L. Farkas, Polarization-sensitive hyperspectral imaging in vivo: A multimode dermoscope for skin analysis. *Sci. Rep.* **4**, 4924 (2015).
5. K. Oka, T. Kato, Spectroscopic polarimetry with a channeled spectrum. *Opt. Lett.* **24**, 1475–1477 (1999).
6. I. J. Vaughn, A. S. Alenin, J. S. Tyo, Channeled spatio–temporal Stokes polarimeters. *Opt. Lett.* **43**, 2768–2771 (2018).
7. M. Alouini, F. Goudail, A. Grisard, J. Bourderionnet, D. Dolfi, A. Bénière, I. Baarstad, T. Løke, P. Kaspersen, X. Normandin, G. Berginc, Near-infrared active polarimetric and multispectral laboratory demonstrator for target detection. *Appl. Optics* **48**, 1610–1618 (2009).
8. M. Garcia, C. Edmiston, R. Marinov, A. Vail, V. Gruev, Bio-inspired color-polarization imager for real-time in situ imaging. *Optica* **4**, 15–18 (2017).
9. A. El Gamal, in *Digest. International Electron Devices Meeting*, (IEEE, 2002), pp. 805–808.
10. R. M. Turner, R. J. Guttosch, Development challenges of a new image capture technology: Foveon X3 image sensors, in *ICIS '06: International Congress of Imaging Science - Final Program and Proceedings* (Society for Imaging Science and Technology, 2006), pp. 175–181.
11. S. Aihara, H. Seo, M. Namba, T. Watabe, H. Ohtake, M. Kubota, N. Egami, T. Hiramatsu, T. Matsuda, M. Furuta, H. Nitta, T. Hirao, Stacked image sensor with green- and red-sensitive organic photoconductive films applying zinc oxide thin-film transistors to a signal readout circuit. *IEEE Trans. Electron Dev.* **56**, 2570–2576 (2009).
12. S. Matthew Menke, R. Pandey, R. J. Holmes, Tandem organic photodetectors with tunable, broadband response. *Appl. Phys. Lett.* **101**, 223301 (2012).
13. V. Pecunia, Efficiency and spectral performance of narrowband organic and perovskite photodetectors: A cross-sectional review. *J. Phys. Mater.* **2**, 042001 (2019).
14. H. Seo, S. Aihara, T. Watabe, H. Ohtake, T. Sakai, M. Kubota, N. Egami, T. Hiramatsu, T. Matsuda, M. Furuta, T. Hirao, A 128 x 96 pixel stack-type color image sensor: Stack of individual blue-, green-, and red-sensitive organic photoconductive films integrated with a ZnO thin film transistor readout ciruit. *Jpn. J. Appl. Phys.* **50**, 024103 (2011).
15. K. H. An, B. O'Connor, K. P. Pipe, M. Shtein, Organic photodetector with spectral response tunable across the visible spectrum by means of internal optical microcavity. *Organic Electronics.* **10**, 1152–1157 (2009).
16. I. Deckman, P. B. Lechêne, A. Pierre, A. C. Arias, All-printed full-color pixel organic photodiode array with a single active layer. *Organic Electronics.* **56**, 139–145 (2018).
17. J. W. Evans, Solc birefringent filter. *J. Opt. Soc. Am.* **48**, 142 (1958).
18. L. Biniek, S. Pouget, D. Djurado, E. Gonthier, K. Tremel, N. Kayunkid, E. Zaborova, N. Crespo-monteiro, O. Boyron, N. Leclerc, S. Ludwigs, M. Brinkmann, High-temperature rubbing : A versatile method to align π-conjugated polymers without alignment substrate. *Macromolecules* **47**, 3871–3879 (2014).
19. J. Marshall, T. W. Cronin, S. Kleinlogel, Stomatopod eye structure and function: A review. *Arthropod Struc. Develop.* **36**, 420–448 (2007).
20. N. J. Marshall, A unique colour and polarization vision system in mantis shrimps. *Nature* **333**, 557–560 (1988).
21. H. H. Thoen, M. J. How, T.-H. Chiou, J. Marshall, A different form of color vision in mantis shrimp. *Science* **343**, 411–413 (2014).
22. M. J. Bok, N. W. Roberts, T. W. Cronin, Behavioural evidence for polychromatic ultraviolet sensitivity in mantis shrimp. *Proc. R. Soc. B* **285**, 20181384 (2018).
23. N. W. Roberts, T. H. Chiou, N. J. Marshall, T. W. Cronin, A biological quarter-wave retarder with excellent achromaticity in the visible wavelength region. *Nature Photonics.* **3**, 641–644 (2009).
24. I. M. Daly, M. J. How, J. C. Partridge, S. E. Temple, N. J. Marshall, T. W. Cronin, N. W. Roberts, Dynamic polarization vision in mantis shrimps. *Nat. Commun.* **7**, 12140 (2016).
25. O. Awartani, M. W. Kudenov, B. T. O'Connor, Organic photovoltaic cells with controlled polarization sensitivity. *Appl. Phys. Lett.* **104**, 093306 (2014).
26. O. Awartani, M. W. Kudenov, R. J. Kline, B. T. O'Connor, In-plane alignment in organic solar cells to probe the morphological dependence of charge recombination. *Adv. Funct. Mater.* **25**, 1296–1303 (2015).
27. P. Sen, R. Yang, J. J. Rech, Y. Feng, C. Hoi, Y. Ho, J. Huang, F. So, R. J. Kline, W. You, M. W. Kudenov, B. T. O. Connor, Panchromatic all-polymer photodetector with tunable polarization sensitivity. *Adv. Optical Mater.* **7**, 1801346 (2019).

28. R. K. Komanduri, K. F. Lawler, M. J. Escuti, Multi-twist retarders: Broadband retardation control using self-aligning reactive liquid crystal layers. *Opt. Express* **21**, 404–420 (2013).
29. S. Gupta Roy, O. M. Awartani, P. Sen, B. T. O'Connor, M. W. Kudenov, Intrinsic coincident linear polarimetry using stacked organic photovoltaics. *Opt. Express* **24**, 14737–14747 (2016).
30. R. M. A. Azzam, Instrument matrix of the four-detector photopolarimeter: Physical meaning of its rows and columns and constraints on its elements. *J. Opt. Soc. Am. A* **7**, 87 (1990).
31. B. Lyot, Optical apparatus with wide field using interference of polarized light. *C. R Acad. Sci.* **4734**, 1593 (1933).
32. K. J. Hornburg, R. K. Komanduri, M. J. Escuti, Highly chromatic retardation via multi-twist liquid crystal films. *J. Optical Soc. Am. B* **36**, D28 (2019).
33. K. S. Whitehead, M. Grell, D. D. C. Bradley, M. Jandke, P. Strohriegl, Highly polarized blue electroluminescence from homogeneously aligned films of poly(9,9-dioctylfluorene). *Appl. Phys. Lett.* **76**, 2946–2948 (2000).
34. H. Tanaka, T. Yasuda, K. Fujita, T. Tsutsui, Transparent image sensors using an organic multilayer photodiode. *Adv. Mater.* **18**, 2230–2233 (2006).
35. M. C. Gather, D. D. C. Bradley, An improved optical method for determining the order parameter in thin oriented molecular films and demonstration of a highly axial dipole moment for the lowest energy π-π^* optical transition in poly(9,9-dioctylfluorene-*co*-bithiophene). *Adv. Funct. Mater.* **17**, 479–485 (2007).
36. M. S. Vezie, S. Few, I. Meager, G. Pieridou, B. Dörling, R. S. Ashraf, A. R. Goñi, H. Bronstein, I. Mcculloch, S. C. Hayes, M. Campoy-Quiles, J. Nelson, Exploring the origin of high optical absorption in conjugated polymers. *Nat. Mater.* **15**, 746–753 (2016).
37. R. Yang, P. Sen, B. T. O'Connor, M. W. Kudenov, Intrinsic coincident full-Stokes polarimeter using stacked organic photovoltaics. *Appl. Optics* **56**, 1768–1774 (2017).
38. J. Choi, W. Kim, D. Kim, S. Kim, J. Chae, S. Q. Choi, F. S. Kim, T.-S. Kim, B. J. Kim, Importance of critical molecular weight of semicrystalline n-type polymers for mechanically robust, efficient electroactive thin films. *Chem. Mater.* **31**, 3163–3173 (2019).
39. R. Zhu, A. Kumar, Y. Yang, Polarizing organic photovoltaics. *Adv. Mater.* **23**, 4193–4198 (2011).
40. K. Tremel, F. S. U. Fischer, N. Kayunkid, R. D. Pietro, R. Tkachov, A. Kiriy, D. Neher, S. Ludwigs, M. Brinkmann, Charge transport anisotropy in highly oriented thin films of the acceptor polymer P(NDI2OD-T2). *Adv. Energy Mater.* **4**, 1301659 (2014).
41. L. Biniek, A. Hamidi-Sakr, L. Grodd, S. Escoubas, Y. J. Dappe, S. Grigorian, M. Schmutz, M. Brinkmann, Structure and charge transport anisotropy of polythieno[3,4-*b*]-thiophene-*co*-benzodithiophene (PTB7) oriented by high-temperature rubbing. *Adv. Electron. Mater.* **4**, 1700480 (2018).
42. X. Wang, L. Lv, L. Li, Y. Chen, K. Zhang, H. Chen, H. Dong, J. Huang, G. Shen, Z. Yang, H. Huang, High-performance all-polymer photoresponse devices based on acceptor–acceptor conjugated polymers. *Adv. Funct. Mater.* **26**, 6306–6315 (2016).
43. X. Xu, X. Zhou, K. Zhou, Y. Xia, W. Ma, O. Inganäs, Large-area, semitransparent, and flexible all-polymer photodetectors. *Adv. Funct. Mater.* **28**, 1805570 (2018).
44. P. Murto, Z. Genene, C. M. Benavides, X. Xu, A. Sharma, X. Pan, O. Schmidt, C. J. Brabec, M. R. Andersson, S. F. Tedde, W. Mammo, E. Wang, High performance all-polymer photodetector comprising a donor–acceptor–acceptor structured indacenodithiophene–bithieno[3,4-*c*]pyrroletetrone copolymer. *ACS Macro Lett.* **7**, 395–400 (2018).
45. Y. Niu, R. Frisenda, E. Flores, J. R. Ares, W. Jiao, D. Perez de Lara, C. Sánchez, R. Wang, I. J. Ferrer, A. Castellanos-Gomez, Polarization-sensitive and broadband photodetection based on a mixed-dimensionality TiS_3 /Si p-n junction. *Advanced Optical Materials.* **6**, 1800351 (2018).
46. L. Ye, P. Wang, W. Luo, F. Gong, L. Liao, T. Liu, L. Tong, J. Zang, J. Xu, W. Hu, Highly polarization sensitive infrared photodetector based on black phosphorus-on-WSe_2 photogate vertical heterostructure. *Nano Energy* **37**, 53–60 (2017).
47. F. Liu, S. Zheng, X. He, A. Chaturvedi, J. He, W. L. Chow, T. R. Mion, X. Wang, J. Zhou, Q. Fu, Highly sensitive detection of polarized light using anisotropic 2D ReS2. *Adv. Funct. Mater.* **26**, 1169–1177 (2016).
48. A. W. Kruse, A. S. Alenin, J. S. Tyo, Review of visualization methods for passive polarization imaging. *Opt. Eng.* **58**, 1 (2019).
49. H. Su, Q. Du, P. Du, Hyperspectral image visualization using band selection. *IEEE J. Select. Topics Appl. Earth Observ. Remote Sens.* **7**, 2647–2658 (2014).
50. N. Strobel, M. Seiberlich, R. Eckstein, U. Lemmer, G. Hernandez-Sosa, Organic photodiodes: Printing, coating, benchmarks, and applications. *Flex. Print. Electron.* **4**, 043001 (2019).
51. P. E. Malinowski, A. Nakamura, D. Janssen, Y. Kamochi, I. Koyama, Y. Iwai, A. Stefaniuk, E. Wilenska, C. Salas Redondo, D. Cheyns, S. Steudel, P. Heremans, Photolithographic patterning of organic photodetectors with a non-fluorinated photoresist system. *Organ. Electron.* **15**, 2355–2359 (2014).
52. Z. Nie, E. Kumacheva, Patterning surfaces with functional polymers. *Nature Mater.* **7**, 277–290 (2008).
53. S.-J. Lim, D.-S. Leem, K.-B. Park, K.-S. Kim, S. Sul, K. Na, G. H. Lee, C.-J. Heo, K.-H. Lee, X. Bulliard, R.-I. Satoh, T. Yagi, T. Ro, D. Im, J. Jung, M. Lee, T.-Y. Lee, M. G. Han, Y. W. Jin, S. Lee, Organic-on-silicon complementary metal–oxide–semiconductor colour image sensors. *Sci. Rep.* **5**, 7708 (2015).
54. M. G. Han, K.-B. Park, X. Bulliard, G. H. Lee, S. Yun, D.-S. Leem, C.-J. Heo, T. Yagi, R. Sakurai, T. Ro, S.-J. Lim, S. Sul, K. Na, J. Ahn, Y. W. Jin, S. Lee, Narrow-band organic photodiodes for high-resolution imaging. *ACS Appl. Mater. Interfaces* **8**, 26143–26151 (2016).
55. A. Hawatky, F. E. Osterloh, A simple laboratory method to pattern sub-millimeter features of conductive films of gold and indium tin oxide. *Instrument. Sci. Tech.* **35**, 53–58 (2007).
56. S.-Y. Lu, R. A. Chipman, Interpretation of Mueller matrices based on polar decomposition. *J. Opt. Soc. Am. A* **13**, 1106 (1996).
57. T. W. Cronin, N. J. Marshall, R. L. Caldwell, *Stomatopod Vision* (Oxford Univ. Press, 2017).
58. Colin, *A Spectrum of Seven Coloured Pencils* (2015); https://commons.wikimedia.org/wiki/File:Seven_Coloured_Pencils_(simulate_Wide_Gamut_display).jpg.
59. J. S. Tyo, Design of optimal polarimeters: Maximization of signal-to-noise ratio and minimization of systematic error. *Appl. Optics* **41**, 619–630 (2002).

Acknowledgments: We thank M. Bok for the use of his mantis shrimp photograph. **Funding:** This work is supported by the NSF under grant no. 1809753. J.R. and W.Y. were supported by the NSF under grant number 1639429. B.J.K. and J.-W.L. acknowledge the support from the National Research Foundation (NRF) grant, funded by the Korean government (NRF-2017M3A7B8065584). **Author contributions:** Conceptualization: M.K., B.T.O., and A.A. Methodology: A.A., P.S., H.S., M.K., and B.T.O. Software: A.A., R.K., and M.K. Validation: A.A., P.S., and H.S. Formal analysis: A.A. and H.S. Investigation: A.A., P.S., H.S., M.K., and B.T.O. Resources: J.R., J.-W.L., M.E., W.Y., B.J.K., R.K., M.K., and B.T.O. Writing—original draft: A.A., P.S., and H.S. Writing—review and editing: A.A., P.S., H.S., J.R., J.-W.L., M.E., W.Y., B.J.K., R.K., B.T.O., and M.K. Visualization: A.A., P.S., H.S., M.K., and B.T.O. Supervision: M.K. and B.T.O. Project administration: M.K., B.T.O., and M.E. Funding acquisition: M.K., B.T.O., M.E., B.J.K., and W.Y. **Competing interests:** The authors declare that they have no competing interests. **Data and materials availability:** All data needed to evaluate the conclusions in the paper are present in the paper and/or the Supplementary Materials. Additional data related to this paper may be requested from the authors.

Submitted 14 August 2020
Accepted 19 January 2021
Published 3 March 2021
10.1126/sciadv.abe3196

Citation: A. Altaqui, P. Sen, H. Schrickx, J. Rech, J.-W. Lee, M. Escuti, W. You, B. J. Kim, R. Kolbas, B. T. O'Connor, M. Kudenov, Mantis shrimp–inspired organic photodetector for simultaneous hyperspectral and polarimetric imaging. *Sci. Adv.* **7**, eabe3196 (2021).